Hindawi
Advances in Materials Science and Engineering
Volume 2022, Article ID 3014060, 13 pages
https://doi.org/10.1155/2022/3014060

Research Article

800 MPa Class HSLA Steel Block Part Fabricated by WAAM for Building Applications: Tensile Properties at Ambient and Elevated (600°C) Temperature

Qian Fang,[1,2] **Lin Zhao**,[2] **Cui-xin Chen**,[1] **Yang Cao**,[2] **Liang Song**,[3] **Yun Peng**,[2] **and Fu-xing Yin**[1]

[1]*Research Institute for Energy Equipment Materials,Tianjin Key Laboratory of Materials Laminating Fabrication and Interfacial Controlling Technology,School of Materials Science and Engineering, Hebei University of Technology, Tianjin 300130, China*
[2]*Central Iron and Steel Research Institute, Beijing 100081, China*
[3]*School of Materials Science and Engineering, Tsinghua University, Beijing 100084, China*

Correspondence should be addressed to Lin Zhao; hhnds@aliyun.com and Fu-xing Yin; yinfuxing@hebut.edu.cn

Received 30 November 2021; Revised 4 January 2022; Accepted 5 January 2022; Published 4 February 2022

Academic Editor: Antonio Riveiro

An 800 MPa class high strength low-alloy (HSLA) steel block part was deposited on substrate with similar composition by gas metal arc welding (GMAW)-based wire arc additive manufacturing (WAAM). The base plate could be removed after deposition or retained as part of the additive manufacturing (AM) part, forming the hybrid additive manufacturing (HAM) part. Tensile tests of the AM part and the HAM part were performed at ambient temperature (AT) and elevated temperature (ET, 600°C held for 4 h) for potential applications in high-rise buildings. Microstructure observations and low temperature impact tests were also conducted. Results show that microstructure of the deposit mainly consists of lower bainite and granular bainite. AT yield strength (YS) of the deposit along the deposition, transverse, and vertical directions is ~770 MPa. ET YS of the deposit along the lateral and building directions could reach 373 MPa, 48.4% of the AT YS. Fracture elongation along all directions could exceed 18.0% for both AT and ET. Low temperature (−50°C) impact absorbed energy of the deposit could exceed 84 J along all directions. Mechanical properties of the HAM part are similar or superior to those of the AM part along the vertical direction, except the AT fracture elongation, which is one-fifth lower. Good strength-ductility-toughness balance of the made part verified the feasibility of using WAAM to manufacture 800 MPa HSLA steel block parts that have potential applications in high-rise buildings, especially considering ET YS of the part might be improved by alloying redesign to meet the performance requirements of building steel.

1. Introduction

Additive manufacturing (AM), a process of joining materials to make objects from 3D model data, usually layer upon layer, as opposed to subtractive manufacturing methodologies (ASTM F2792-12a), has gained great progress since the later 1980s. AM process can manufacture termination parts directly with/without postmachining, greatly decreasing the lead time and manufacturing cost and increasing the material utilization [1]. Metal AM is commonplace in aerospace, automotive, energy, and medical industries. It is anticipated that these industries will share 84% of the AM market by 2025 [2].

Wire and arc additive manufacturing (WAAM), in which metal wire has been selected as the feedstock and high energy efficiency electronic arc has been selected as the heat source to melt metal wire as well as base metal and deposits metal layer by layer to fabricate a metal structure [3, 4], has emerged in the beginning of the last century [5]. Wire feedstock makes WAAM process cost-effective and environment friendly as well as high material utilizing [6]. Compared with other AM technologies, WAAM is identified

by significantly great deposition rate (3–10 kg/h), unlimited building envelope, and low capital cost [7]. All these characteristics make WAAM suitable to fabricate fully dense near-net-shaped metallic components for building applications with high forming efficiency at a low investment [8] and maximize the design freedom [9]. Recently, WAAM has been successively applied to construction industries, for example, an excavator arm [10] and 10.5 m span footbridge [11] have been manufactured by WAAM and passed the service test.

High-strength low-alloy (HSLA) steels that contain small amounts of carbon (<0.25 wt.%) combined with trace alloying elements [12] are widely used in a variety of industries, such as naval and automotive [13], ship building and offshore platforms [14], and transportation and construction [15], due to their excellent mechanical properties and low cost. However, research on WAAM of HSLA steels largely lays behind until recent years [16, 17]. Dai et al. [18] successively manufactured a high-building multidirectional pipe joint (HBMDPJ) through space surface slicing method and space path planning, with dimensional errors approximately ±1 mm and angle errors of no more than ±0.5°. The tensile strength and impact toughness (20°C) of the WAAM fabricated HSLA steel part increased by 12.4% and 100%, respectively, compared with those of its casting counterpart. By studying the microstructure characteristics and transformation of the HBMDPJ fabricated by WAAM, the authors [19] found four distinguishing regions in the forming part, consisting of the solidification zone, the complete austenitizing zone, the partial austenitizing zone, and the tempering zone, that had a distinct thermal history and hence microstructure. Rafieazad et al. [8] found uniform microstructure of ER70S-6 block fabricated by WAAM containing mainly ferrite in the horizontal direction and 45° to the deposition direction in building plain as well as isotropic tensile and impact properties, resulting from a stripe deposition strategy, with a 90° rotation between successive layers of the deposited part. They also found inferior tensile mechanical properties along the vertical direction. Nabulsi et al. [20] prepared large-sized steel components using WAAM and compared their mechanical properties with EN 8 carbon mild steel. Mechanical properties of the WAAM steel satisfied the requirements for a building steel grade for building structures as specified by Eurocode 3(EN 1993-1-1).

The requirements for performance of high-rise building steel parts have increased from 490 MPa and 590 MPa to 780 MPa [21], and their requirements for fracture elongation are 23.0%, 20.0%, and 16.0%, respectively. However, there are few reports concerning 780 MPa steel parts fabricated by WAAM. In this study, welding wire of 785 MPa class steel and gas metal arc welding (GMAW)-based WAAM were used to manufacture an 800 MPa class HSLA steel block part on the 785 MPa steel substrate. The base plate could be removed after deposition or retained as part of the additive manufacturing (AM) part, forming the hybrid additive manufacturing (HAM) part. Tensile properties of the AM part and the HAM part were tested and investigated at ambient temperature (AT) and elevated temperature (ET, 600°C held for 4 hours) for potential applications in high-rise building. Microstructure observations and low temperature (−50°C) impact tests were also performed and analysed.

2. Experimental

2.1. Part Fabrication. A WAAM system (Figure 1(a)) was used to deposit the part (Figure 1(b)) on the substrate following a parallel deposition strategy (Figure 1(c)). The WAAM system was composed of a 6-axis robot equipped with a 2-axis positioner and welding system. A gas metal arc welding (GMAW) heat source was used to melt the wire as well as the substrate to realize the manufacturing process. A commercial welding wire (Φ1.2 mm) designed for 785 MPa class high strength steel was used. Dimension of the substrate plate is $500 * 120 * 60$ mm. Microstructure of the substrate steel is tempering martensite. Ultimate tensile strength (UTS), yield strength (YS), and fracture elongation (El) of the substrate are 880 MPa, 820 MPa, and 22.0%, respectively. Compositions of the wire and substrate are listed in Table 1. The substrate was cleaned with acetone and dried before deposition. The interlayer and interpass temperature during deposition was controlled at 100–120°C with the help of a portable thermal couple. The shielding gas was 5% CO_2+95% Ar. A centre to centre strategy between layers was adopted. After deposition of one layer had been finished, the torch ascended a height accordingly for the deposition of the next layer until the designed feature was obtained (Figure 1(b)). An overlap ratio 50% for neighbouring passes was adopted. The deposition parameters are listed in Table 2.

2.2. Microstructure Observation. Metallurgical samples were cut by wire electrical discharge machining (WEDM), ground, and polished before etching by 4% nital for optical microscope (OM), scanning electron microscope (SEM) observations, and microhardness test. A disc like sample with thickness of 200 μm was WEDM cut from the deposit at random and ground to 40–50 μm thick before twin-jet electropolished in 6% perchloric alcohol solution for transmission electron microscope (TEM) observations. An $8 * 5 * 1$ mm sample was cut, ground, polished, and electrlytically polished for EBSD characterization (step size, 0.2 μm). The metallurgical sample had also been put into aqueous solution of saturated picric acid (60°C for 2 minutes) to reveal the macrostructure of the deposited passes.

2.3. Mechanical Properties Characterization. Dog-bone like tensile test samples (M12Φ5) were removed from the AM part along the deposition, transverse, and vertical directions (Figure 2(a)), which are denoted by *X*, *Y*, and *Z*, respectively, hereafter. Two samples were tested for the average value per direction at ambient and elevated temperatures (600°C, held for 4 hours). Full size ($55 * 10 * 10$ mm) impact test samples with V notch were extracted from the deposit along *X*, *Y*, and *Z* (Figure 2(b)). Instrumented Charpy impact test was performed three times per condition for the average value at −50°C. Tensile mechanical properties and impact toughness of the HAM part were also investigated, and the sampling

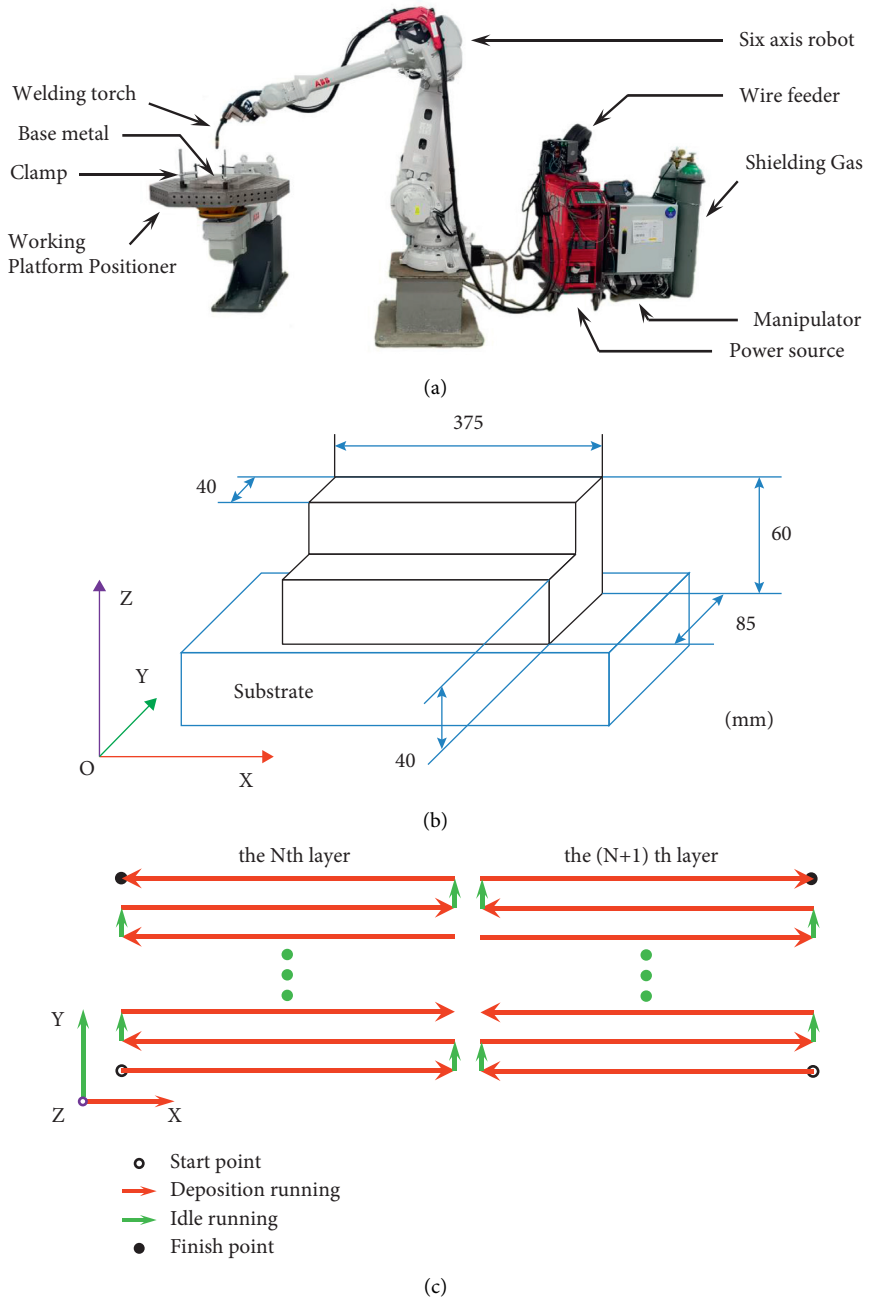

Figure 1: The WAAM system and manufacturing of the deposit. (a) The WAAM system; schematic illustrations of the (b) deposit and (c) deposition strategy.

Table 1: Compositions of the wire and substrate (wt.%).

Element	C	Mn	Si	(Cr + Ni + Mo)	(V + Ti + Al)	Fe
Wire	0.07	1.70	0.45	3.80	0.060	Bal.
Substrate	0.10	0.56	0.24	5.50	-	Bal.

Table 2: Process parameters of the deposition.

Torch travel speed (mm/min)	Wire feed speed (m/min)	Voltage (V)	Current (A)	Shielding gas flow rate (L/min)
5	9	26.8	286	20

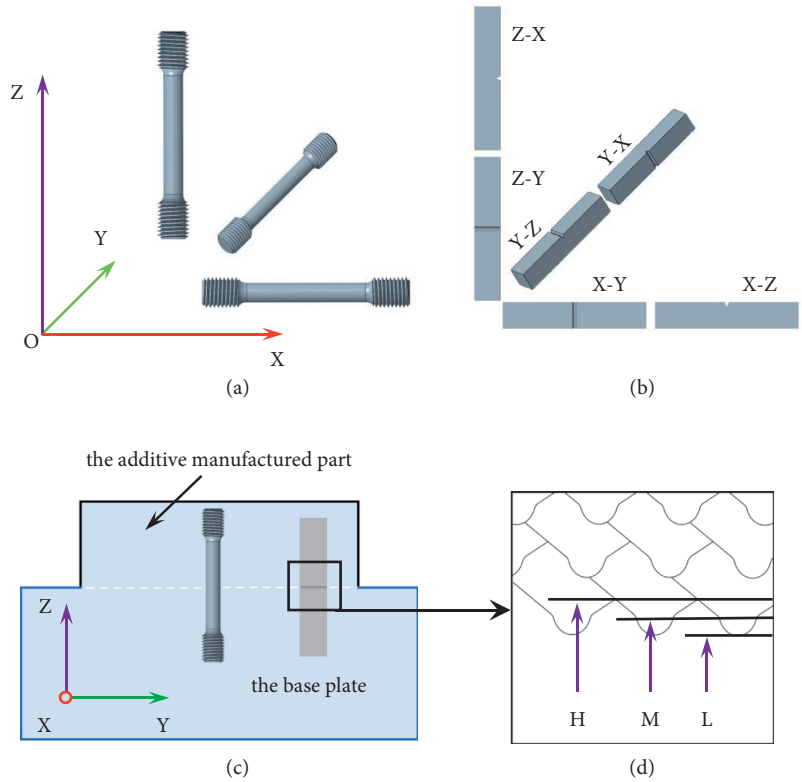

FIGURE 2: Schematic illustrations of sampling locations. (a) Tensile tests, (b) impact test sampling of the AM part, (c) tensile and impact test sampling locations, and (d) V notch locations of impact test samples of the HAM part.

locations are shown in Figure 2(c). Impact tests (−50°C) were performed on samples extracted from HAM part with the *V* notch located at different locations, which were denoted by *H*, *M*, and *L* (Figure 2(d)). The microhardness indentation was performed on metallurgical sample with a load of 200 g (dwell time, 10 s) and the step size was 200 μm.

3. Results and Discussions

3.1. Macro- and Microstructure. Figure 3 shows the macrostructure of the deposit during and after deposition. The deposition strategy adopted in this study can effectively compensate the height difference at the arc starting and ending of a pass, preventing the part from collapsing (Figure 3(a)) [22]. A flat building plain could be achieved under a 50% overlap ratio. Figures 3(b) and 3(c) indicate the deposit after deposition had been finished. The deposit shape is relatively regular as design (Figure 1(b)), which further conforms the effectiveness of the deposition strategy and selection of overlap ratio on shape control.

Figure 4 reveals microstructure of the deposit. Figure 4(a) is a 3-D view of a cubic sample composed of several passes removed from the deposit. There are no obvious defects, such as porosity, pores, or cracks, in the deposit, which indicates a nearly 100% dense part was obtained. Figure 4(b) is a cross-section of several passes from the YOZ view. The cross-section of a trial perpendicular to the deposition direction is clearly enclosed by the vicinity passes, which is defined as the deposit unit hereafter. The deposition sequence is from bottom to top and from right to left, which could be identified by the morphology of the trial cross-section. The deposit unit could be divided into four regions according to the microstructure morphology, which is decided by the thermal cycles experienced, i.e., the fine cellular grain region, the equiaxial grain region, the column grain region, and the coarse grain region, which are denoted by *f*, *c*, *d*, and *e* in white solid boxes (Figure 4(b)). The fine grain region locates at the bottom of the deposit unit, which was formed under a rapid cooling rate, and is mainly composed of lower bainite (LB) (Figure 4(f)) [23]. The equiaxial grain region locates at the upper of the deposit unit on the positive side of *Y* direction (the pass increasing direction in the building plain) and is consisted of lower bainite and granular bainite (GB) (Figures 4(c) and 4(g)). The column grain region, which is the predominant part of the deposit unit, locates at deposit unit on the negative side of *Y* direction and is mainly LB and trace amount of GB (Figures 4(d) and 4(h)). The coarse grain region, with the grain size probably as large as hundreds of micrometers, was formed by the overheating effect of the following passes, and was distributed near the boundaries (fusion lines) of the deposit unit and the following passes. The microstructure of coarse grain is a mixture of LB and GB (Figures 4(e) and 4(i)). Figure 4(j) shows the EBSD result, and the effective grain size is approximately 2.50 μm, which could be the size of a bainite block or packet [24], consisting of a high dislocation density bainite lath (Figure 4(k)) with small disorientations.

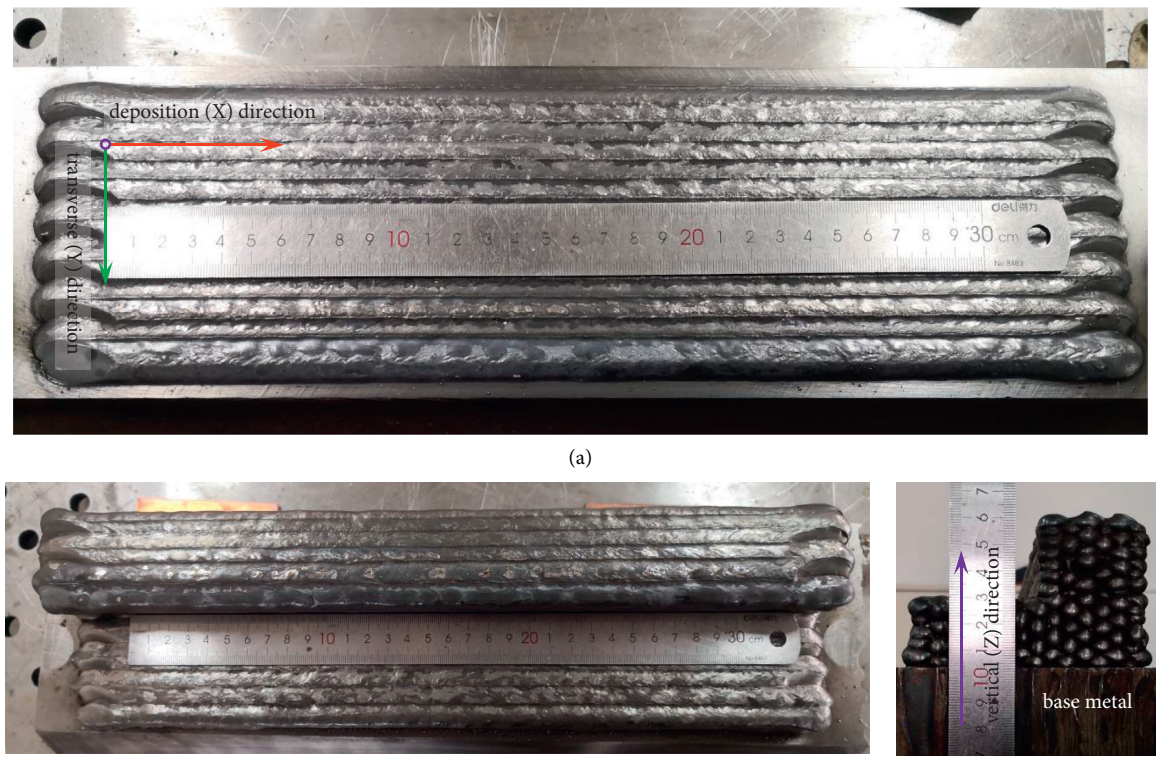

Figure 3: Macroscopic morphology of the deposit. (a) Top view after the first layer had been finished; (b) top and (c) side views of the made part.

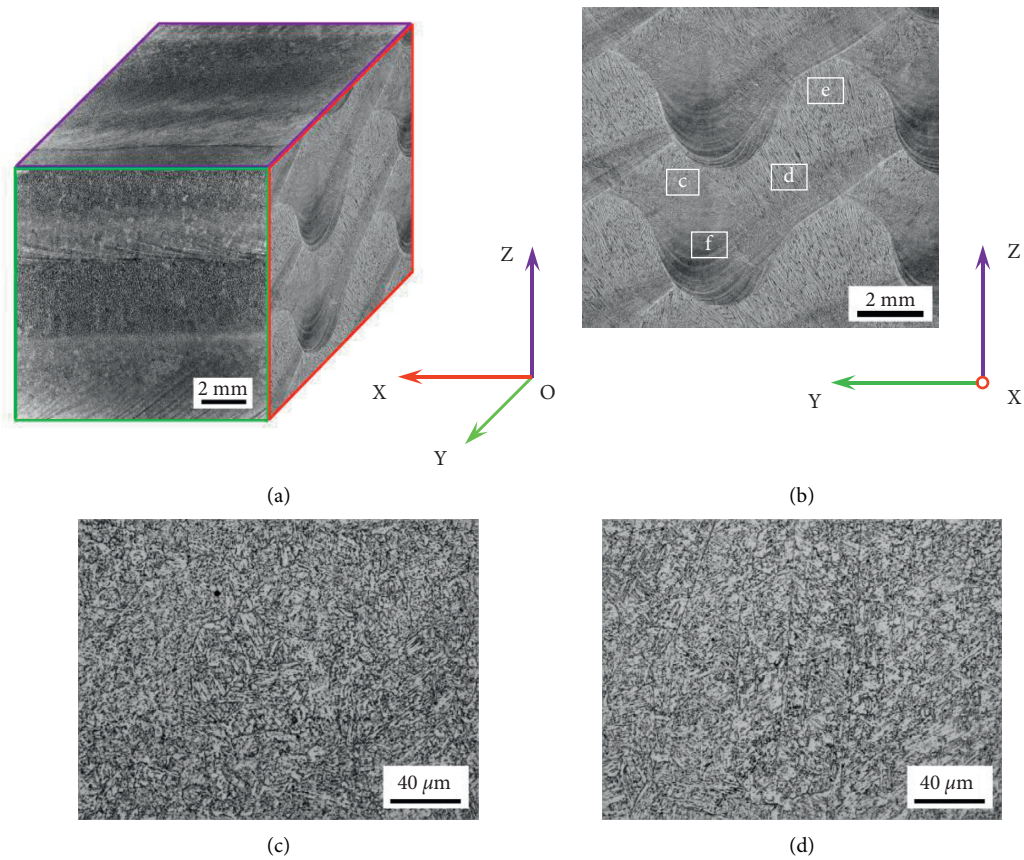

Figure 4: Continued.

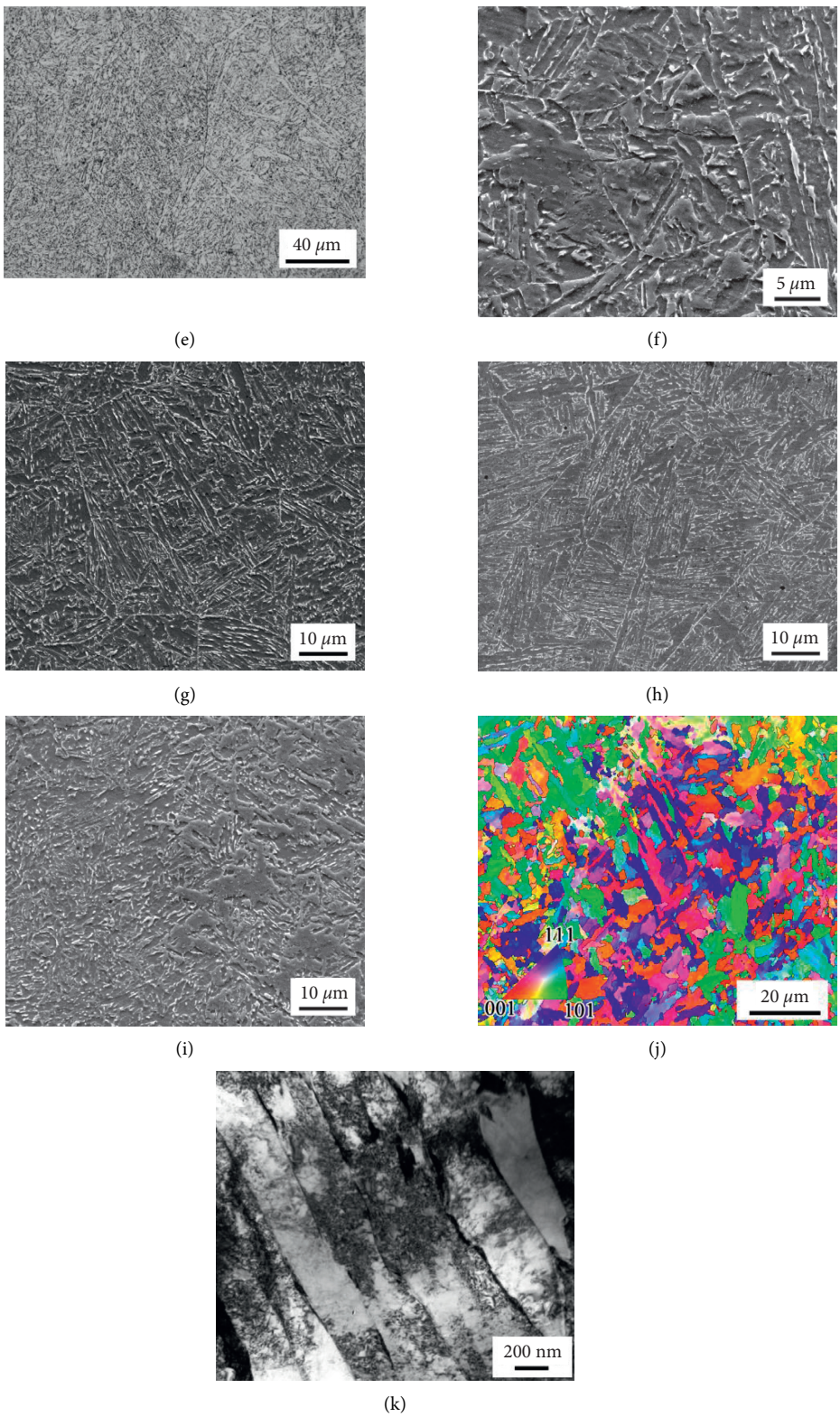

Figure 4: Microstructure of the deposit. (a) 3-D view of several passes; (b) YOZ view of passes; (c–e) OM and (f–i) SEM of the deposit; (c, g) equiaxial grain; (d, h) column grain; (e, i) coarse grain; (f) fine cellular grain; (j) IPF of a column grain (EBSD); (k) bainite laths (TEM).

3.2. Mechanical Properties

3.2.1. Tensile Properties of the Deposit at Ambient and Elevated Temperatures. Ambient temperature (AT) ultimate tensile strength (UTS) of the deposit along X is 852 ±1.5 MPa, slightly higher than that along Y and Z, which are 828 ± 0.5 MPa and 846 ± 0.5 MPa, respectively. Yield strength (YS) of the deposit along X, Y, and Z is 767 MPa, 770 MPa, and 771 MPa, respectively (Figure 5(a)), meeting the requirements of small yield strength fluctuations for the fire proof properties of building steel. The fracture elongation (El) along X is 21.8%, approximately one-fifth higher than that along Y and Z, which are 18.5% and 18.0%, respectively (Figure 5(a)).

Elevated temperature UTS and YS of the deposit along X are 409 MPa and 319 MPa, respectively, inferior to that along Y and Z, which are 450 MPa and 372 MPa, respectively. The fracture elongation along X is 25.8%, approximately two-fifths higher than that along Y and Z, which are 18.5% and 18%, respectively (Figure 5(b)). Elevated temperature yield strength of the deposit is 41.6–48.3% of the ambient temperature yield strength, lower than the requirement of fire proof steel, which requires that the ET YS remains two-thirds of the AT YS [25]. It should be noted that the wire used in this study is designed for gas metal arc welding of 785 MPa class HSLA steel, and the tensile properties at elevated temperature might be improved by alloying redesigning of the wire, such as adding proper amounts of Ni and Mo, which benefit high temperature tensile properties as solid solution strengthening elements [26].

Tensile properties of the deposit along X follow a strength-ductility trade-off relationship when comparing ET tensile properties with the AT tensile properties, which sacrifices strength to obtain a higher fracture elongation, or vice versa, as shown in Figures 5(c) and 5(d). Nevertheless, the fracture elongation along Y and Z did not change while the UTS and YS dropped from 840 MPa and 770 MPa to 450 MPa and 370 MPa (Figures 5(c) and 5(d)) when the test temperature was elevated to 600°C.

The tensile property anisotropies and differences between room and elevated temperatures could be explained by the microstructure and microhardness distribution nonuniformity (Figures 6(a) and 6(b)) [25]. From the YOZ view, the deposition unit could be divided into several regions according to microhardness values: the average value region (299 ± 20HV), the softened region (<279HV), and the hardened region (>319HV), and their area ratios are 74.5%, 15.9% and 9.6%, respectively. The softened regions locate mainly the meeting region of the deposition unit and following passes (Figures 6(a) and 6(b)). The softened region is mainly coarse grains caused by the following overheating. The hardened region is mainly the fine grains caused by the 1150°C reheating thermal cycle [28] and the fine grains in the vicinity of the bottom fusion line. The distribution of the softened and hardened regions is parallel to X, along the fusion line of the deposit, and changed periodically from the view of YOZ for the deposition units share similar thermal history.

The hardness distribution can determine the behavior of tensile test samples while loaded. For samples along the deposition direction, every region distributes consecutively along the longitudinal direction of the samples, as shown in Figures 6(c) and 6(d). While for samples along the lateral and building directions, different regions change periodically along the longitudinal axis of the tensile sample, separating the sample into hardness heterogeneous parts, as shown in Figures 6(e) and 6(f). Stress concentrate occurs at the softened regions at the very beginning of the tensile test [29]. A competing fracture mechanism makes an immature failure, resulting in inferior elongation of the lateral and building directions and superior fracture elongation along the deposition direction.

Figure 7 indicates the fractography of tensile test samples. Figures 7(a)–7(c) reveal the fractography of ambient temperature tensile test sample along X of the made part. The typical cup-cone fractography consists of fiber region with deep and uniformly distributed dimples (Figure 7(c)), radiation region, which is a ~20 μm circular ring enclosing the fiber region with shallow dimples, and shear lip, which is composed of deep dimples (Figure 7(b)). These characteristics contribute to the high room temperature fracture elongation (21.8%) along X. While the shear lip along the other two directions is composed of shallow dimples, resulting in inferior fracture elongation (~18.0%). Figures 7(d)–7(f) reveal the fractography of elevated temperature tensile test sample lateral direction of the deposit along Z. The cup-cone shape fractography also consists of fiber region, radiation region, and shear lip (Figure 7(d)). The fiber region is composed of deep and big dimples (Figure 7(f)), while the radiation region consists of up-open shallow dimples (Figure 7(e)). The sample fractography along Y shares the same feature with Z. These characteristics contribute to the inferior elongation (18.0%) of tensile samples along Y and Z. While the fracture shear lip of the deposit along X is composed of dimples, resulting in superior elongation (25.8%).

3.2.2. Low Temperature (−50°C) Toughness of the Deposit. Figure 8 indicates the impact property and the fractography of the deposit. The average absorbed energy along X is 84 J, inferior to that along Y and Z, which are 108 J and 113 J, respectively, as shown in Figure 8(a). Figure 8(b) reveals the typical load-displacement curve of samples along X and Y. The main difference between the two samples is the characteristic point Fm, which represents the maximum force while loaded. Sample along Y has a higher Fm at a longer displacement, as shown in Figure 8(c). Figures 8(d)–8(f) reveal the sample fractography along Y, denoted by Y-Z-1. The crack experienced a long distance of 2180 μm ductile region before transformed to cleavage region (Figures 8(d)–8(e)), and the ductile region is uniformly distributed with deep dimples (Figure 8(f)). X-Z-1 experienced a short ductile region of 821 μm and then entered the quasicleavage region (Figures 8(g)–8(h)). The secondary cracks and quasicleavage also contribute to the high absorbed energy of X-Z-1. The impact properties of the deposit meet the requirements of fire proof steel for high-rise building, which is 27 J at −40°C [25].

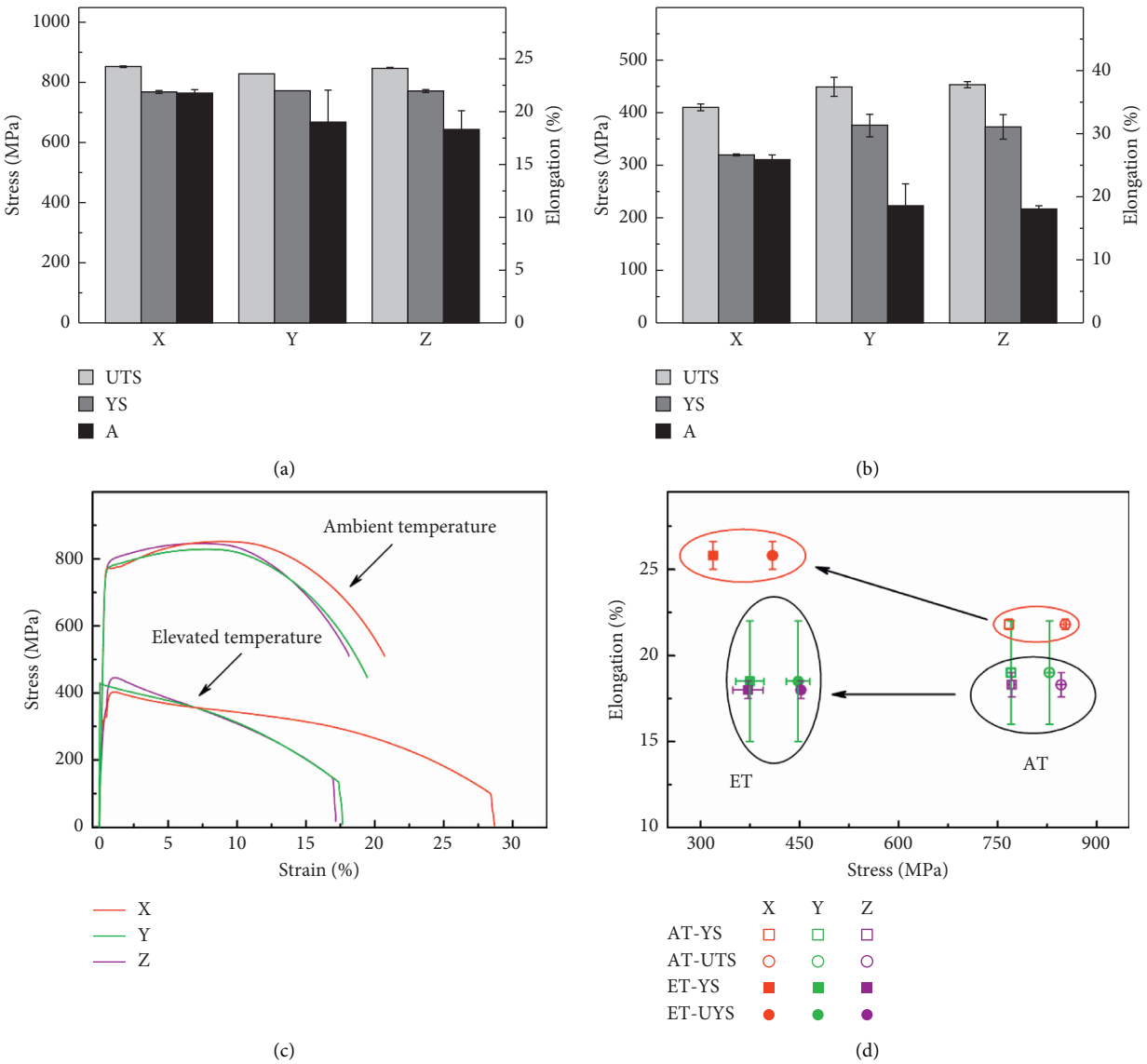

Figure 5: Tensile properties of the deposit. (a) Ambient and (b) elevated temperature tensile properties; (c) stress-strain curves; (d) comparison of ambient and elevated temperature tensile properties.

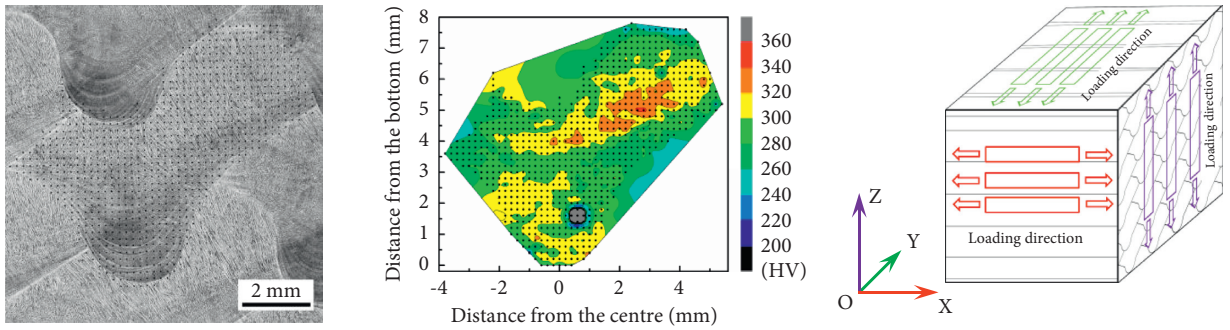

Figure 6: Continued.

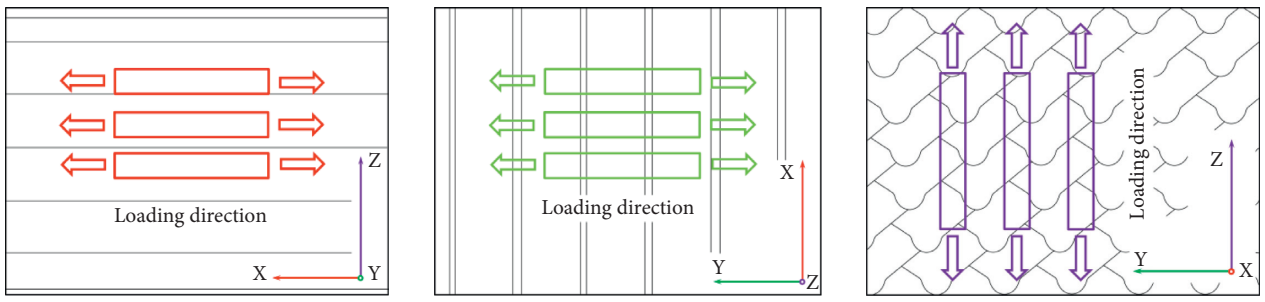

Figure 6: Microhardness distribution and schematic sampling locations of tensile test. (a) Test points distribution of microhardness; (b) microhardness distribution cloud map; (c) sampling locations of tensile test sample from a 3-D view; sampling locations of tensile test sample along (d) *X*, (e) *Y*, and (f) *Z*.

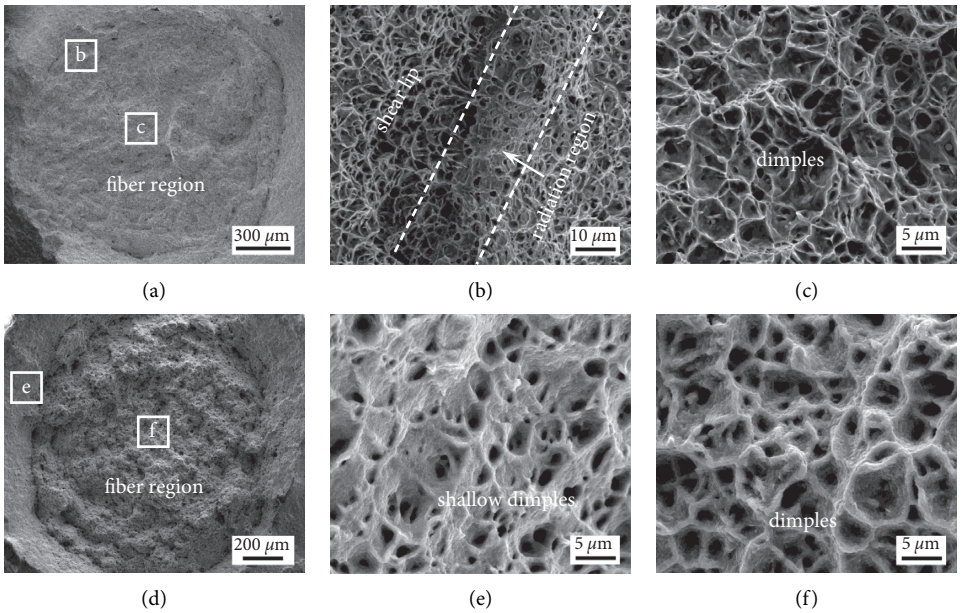

Figure 7: Fractography of the tensile test samples. (a, d) Macroscopic fractography; (b, c), (e, f) microscopic fractography; (a–c) ambient temperature tensile test fractography along X; (d–f) elevated temperature test fractography along Z.

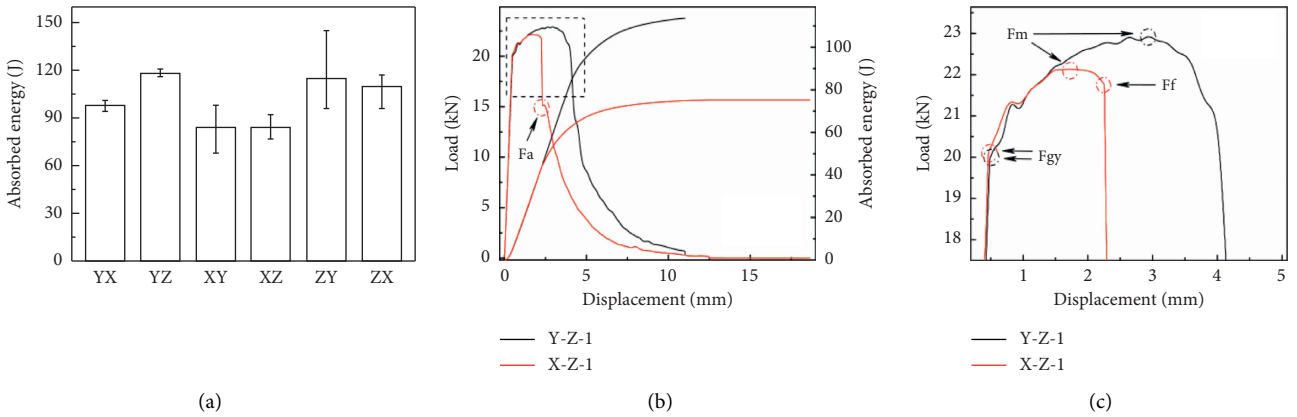

Figure 8: Continued.

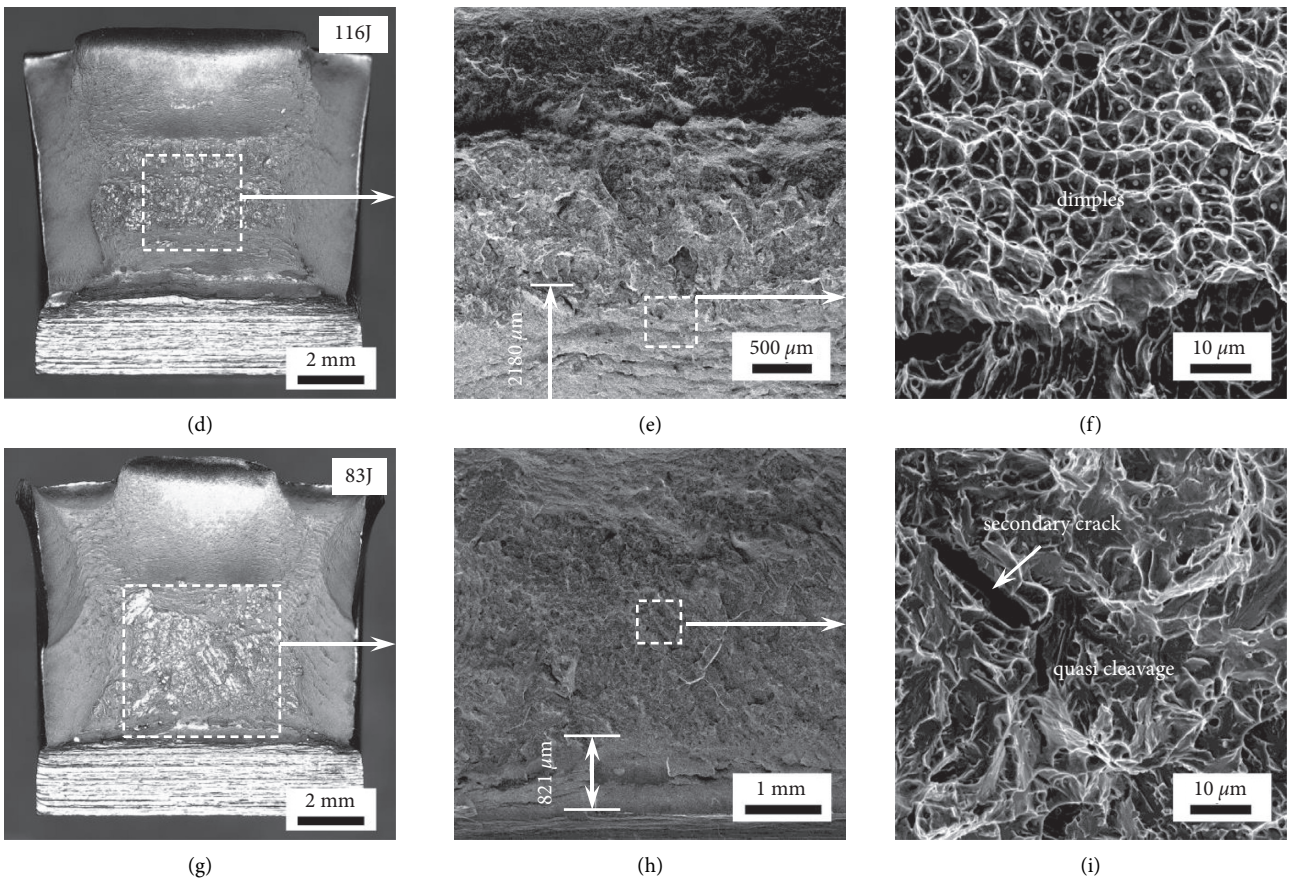

Figure 8: Properties and fractography of impact tests. (a) Impact absorbed energy; (b) typical load-displacement curves of the deposit; (c) enlarged image of the rectangle enclosed by white dashed line in (b); macroscopic (d) and microscopic (e, f) morphology of Y-Z-1; macroscopic (g) and microscopic (h, i) morphology of X-Z-1.

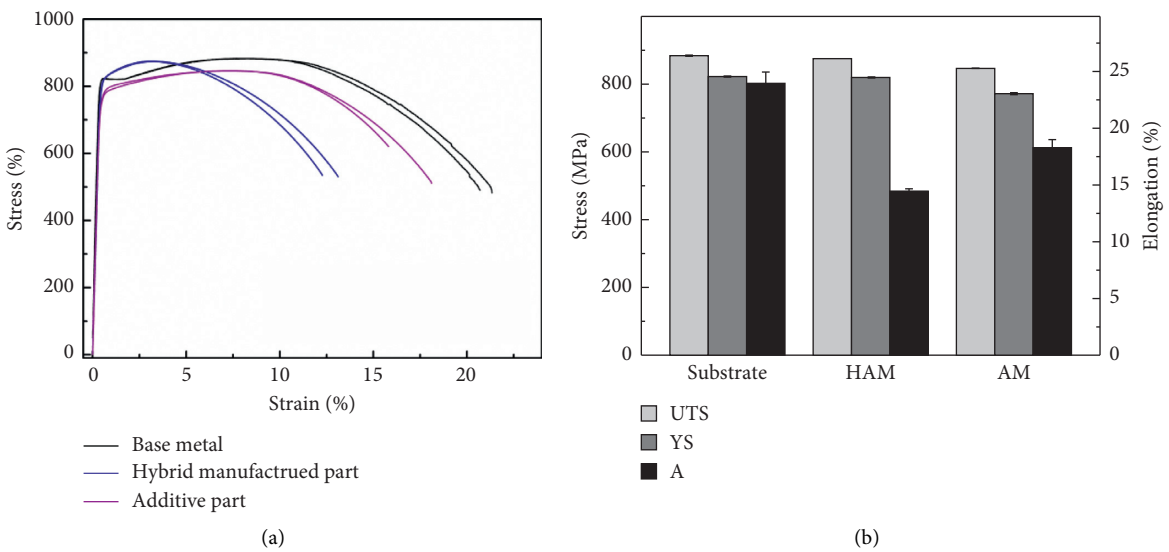

Figure 9: Continued.

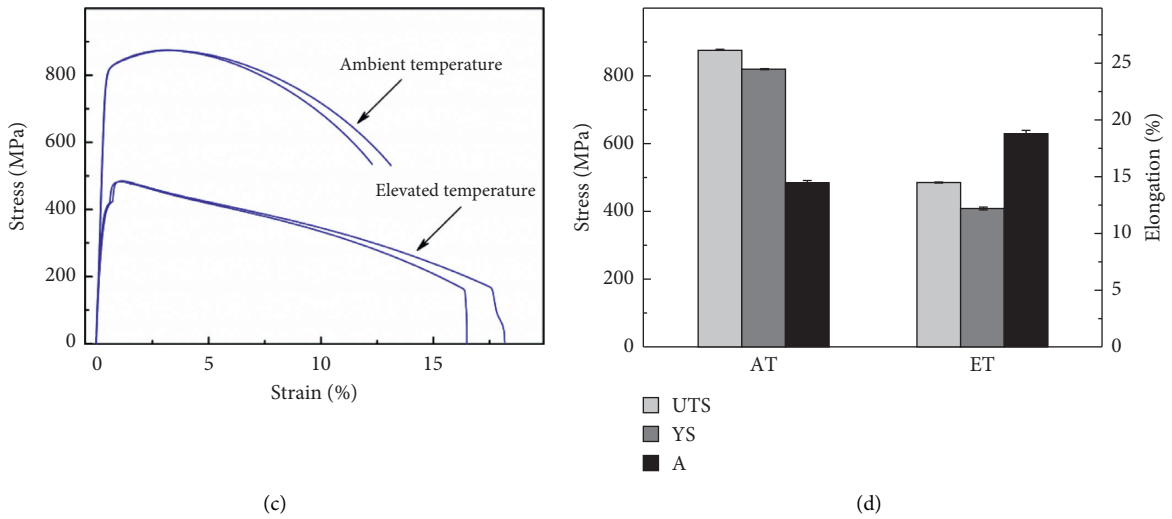

Figure 9: Tensile properties of HAM part. (a) Strain-stress curves and (b) comparison of tensile properties of substrate, AM, and HAM part at ambient temperature; (c) strain-stress curves and (d) comparison of tensile properties of HAM part at ambient temperature and elevated temperature.

3.2.3. Mechanical Properties of the Additive Manufacturing Deposit-Substrate Conjunction. Figure 9 reveals the tensile properties of HAM part at room and elevated temperatures. The AT UTS and YS are 875 MPa and 819 MPa, respectively, nearly the same as the substrate, which are 880 MPa and 820 MPa, respectively. However, the fracture elongation is 14.5%, greatly deteriorated compared with that of AM part and substrate, which are 18.3% and 24%, respectively, as shown in Figures 9(a)–9(b). The ET UTS and YS decrease to 484 MPa and 407 MPa (Figures 9(c)–9(d)), respectively, approximately 30 MPa higher than that of the AM part along Z. The fracture elongation at elevated temperature is 18.8%, increased by one-third compared with that at room temperature. The fractography features of the HAM part share the same characteristics with the building direction fractography. Excellent composition and property compatibility of the wire and substrate (Table 1) guarantee the tensile property compatibility of the deposit and substrate. Absorbed energy of the HAM part with different V notch locations, which are denoted by *L*, *M*, and *H*, is 153 J, 127 J, and 113 J, respectively. With the V notch close to the substrate, the impact absorbed energy increases, resulting from higher Ni content for adjoining the high Ni content substrate (Table 1), which is beneficial to improve the low temperature toughness [30].

4. Conclusions

Welding wire of 785 MPa HSLA steel and GMAW-WAAM was adopted to manufacture a block part. Ambient temperature and elevated temperature (600°C, held for 4 hours) tensile tests of the AM part and the HAM part were performed for potential applications as fire proof steel parts in high-rise buildings. Microstructure observations and low temperature (−50°C) impact tests were also conducted. Conclusions could be drawn as follows:

(1) An 800 MPa class HLSA steel dense block part was fabricated by GMAW-based WAAM at a deposition rate of 4.5 kg/h. Microstructure of the dense part is a mixture of lower bainite and granular bainite.

(2) The AM part occupies good strength-ductility balance at ambient temperature. The UTS, YS, and fracture elongation are 830–850 MPa, 765–770 MPa, and 18.3–22.8%, respectively.

(3) The elevated temperature UTS, YS, and fracture elongation of the AM part are 409–450 MPa, 319–370 MPa, and 18.0–25.8%, respectively.

(4) The AM part has a good low temperature toughness of 80–120J (−50°C).

(5) The additive part combines well with the substrate both at ambient temperature and elevated temperature. The UTS, YS, fracture elongation, and low temperature absorbed energy of the HAM part exceed for those of the AM part, except the ambient temperature fracture elongation, which is 14.5%, one-fifth lower than that of the AM part.

Mechanical properties of the AM/HAM part fabricated by GMAW-WAAM nearly meets all performance requirements for fire proof steel part of high-rise building, except the yield strength at elevated temperature, verifying the feasibility of adopting WAAM to manufacture 800 MPa class high strength block parts used in building industry. Although the elevated temperature yield strength did not remain two-thirds of the ambient temperature yield strength, it might be resolved by alloy redesign of the wire, such as adding proper amounts of Ni [30] and Mo [26].

Data Availability

The data used to support the findings of this study are included within the supplementary information files.

Additional Points

An 800 MPa class HSLA steel block part was fabricated by WAAM at a deposition rate of 4.5 kg/h; yield strength at room temperature and 600°C (4 h) is 770 MPa and 374 MPa, respectively, with good ductility (18.0%). Mechanical properties of the made part nearly meet all performance requirements of building steels.

Conflicts of Interest

The authors declare that there are no conflicts of interest regarding the publication of this article.

Authors' Contributions

Qian Fang conceptualized the study, investigated the study, curated the data, and wrote the original draft. Lin Zhao did the funding acquisition. Cui-xin Chen and Yang Cao reviewed and edited the manuscript. Liang Song visualized the study. Yun Peng did project administration. Fu-xing Yin supervised the study.

Acknowledgments

The authors would like to thank Dr. Dayue Zhang and Hongjian Zhao for proof reading this article. This work was supported by the National R&D Program of China (grant nos. 2017YFB1103700 and 2017YFB1103703) and the Joint Doctoral Training Foundation of Hebei University of Technology (grant no. 2018GN003).

Supplementary Materials

Figure 1: screenshot of original data of tensile tests at elevated temperature. Figure 2: screenshot of original data of tensile tests at ambient temperature. Figure 3: screenshot of original data of tensile tests of the hybrid-additive manufacturing part. (*Supplementary Materials*)

References

[1] W. E. Frazier, "Metal additive manufacturing: a review," *Journal of Materials Engineering and Performance*, vol. 23, no. 6, pp. 1917–1928, 2014.

[2] A. S. Yildiz, K. Davut, B. Koc, and O. Yilmaz, "Wire arc additive manufacturing of high-strength low alloy steels: study of process parameters and their influence on the bead geometry and mechanical characteristics," *International Journal of Advanced Manufacturing Technology*, vol. 108, no. 11-12, pp. 3391–3404, 2020.

[3] P. Baker, *Method of Making Decorative Articles*, US, 1925, https://www.freepatentsonline.com/3324213.html.

[4] Z. Zeng, B. Q. Cong, J. P. Oliveira et al., "Wire and arc additive manufacturing of a Ni-rich NiTi shape memory alloy: microstructure and mechanical properties," *Additive Manufacturing*, vol. 32, Article ID 101051, 2020.

[5] W. C. Ke, J. P. Oliveira, B. Q. Cong et al., *Additive Manufacturing*, vol. 50, Article ID 102513, 2020.

[6] D. Ding, Z. Pan, D. Cuiuri, and H. Li, "Wire-feed additive manufacturing of metal components: technologies, developments and future interests," *International Journal of Advanced Manufacturing Technology*, vol. 81, no. 1-4, pp. 465–481, 2015.

[7] J. Liu, Y. Xu, Y. Ge, Z. Hou, and S. Chen, "Wire and arc additive manufacturing of metal components: a review of recent research developments," *International Journal of Advanced Manufacturing Technology*, vol. 111, no. 1-2, pp. 149–198, 2020.

[8] M. Rafieazad, A. V. Nemani, M. Ghaffari, and A. Nasiri, "On microstructure and mechanical properties of a low-carbon low-alloy steel block fabricated by wire arc additive manufacturing," *Journal of Materials Engineering and Performance*, vol. 30, no. 7, pp. 4937–4945, 2021.

[9] H. Lockett, J. L. Ding, S. Williams, F. Martina, and J. Eng, "Design for Wire + Arc Additive Manufacture: design rules and build orientation selection," *Journal of Engineering Design*, vol. 28, pp. 568–598, 2017.

[10] C. Greer, A. Nycz, M. Noakes et al., "Introduction to the design rules for metal big area additive manufacturing," *Additive Manufacturing*, vol. 27, pp. 159–166, 2019.

[11] L. Gardner, P. Kyvelou, G. Herbert, and C. Buchanan, "Testing and initial verification of the world's first metal 3D printed bridge," *Journal of Constructional Steel Research*, vol. 172, Article ID 106233, 2020.

[12] T.-B. An, J.-S. Wei, L. Zhao, J.-G. Shan, and Z.-L. Tian, "Influence of carbon content on microstructure and mechanical properties of 1000 MPa deposited metal by gas metal arc welding," *Journal of Iron and Steel Research International*, vol. 26, no. 5, pp. 512–518, 2019.

[13] V. R. Duate, T. A. Rodrigues, N. Schell, T. G. Santos, J. P. Oliveira, and R. M. Miranda, "Wire and arc additive manufacturing of high-strength low-alloy steel: microstructure and mechanical properties," *Advanced Engineering Materials*, vol. 23, no. 11, Article ID 2001036, 2021.

[14] A. Vahedi Nemani, M. Ghaffari, and A. Nasiri, "Comparison of microstructural characteristics and mechanical properties of shipbuilding steel plates fabricated by conventional rolling versus wire arc additive manufacturing," *Additive Manufacturing*, vol. 32, Article ID 101086, 2020.

[15] C. Buchanan and L. Gardner, "Metal 3D printing in construction: a review of methods, research, applications, opportunities and challenges," *Engineering Structures*, vol. 180, pp. 332–348, 2019.

[16] P. Bajaj, A. Hariharan, A. Kini, P. Kürnsteiner, D. Raabe, and E. A. Jägle, "Steels in additive manufacturing: a review of their microstructure and properties," *Materials Science and Engineering A*, vol. 772, Article ID 138633, 2020.

[17] H. Fayazfar, M. Salarian, A. Rogalsky et al., "A critical review of powder-based additive manufacturing of ferrous alloys: process parameters, microstructure and mechanical properties," *Materials & Design*, vol. 144, pp. 98–128, 2018.

[18] Y. L. Dai, S. F. Yu, Y. S. Shi, T. Y. He, and L. C. Zhang, "Wire and arc additive manufacture of high-building multi-directional pipe joint," *International Journal of Advanced Manufacturing Technology*, vol. 96, pp. 2389–2396, 2018.

[19] Y.-l. Dai, S.-f. Yu, A.-g. Huang, and Y.-s. Shi, "Microstructure and mechanical properties of high-strength low alloy steel by wire and arc additive manufacturing," *International Journal of Minerals, Metallurgy and Materials*, vol. 27, no. 7, pp. 933–942, 2020.

[20] Z. Al-Nabulsi, J. T. Mottram, M. Gillie, N. Kourra, and M. A. Williams, "Mechanical and X ray computed tomography characterisation of a WAAM 3D printed steel plate for structural engineering applications," *Construction and Building Materials*, vol. 274, Article ID 121700, 2021.

[21] W. Sha, F. S. Kelly, and Z. X. Guo, "Microstructure and properties of nippon fire-resistant steels," *Journal of Materials Engineering and Performance*, vol. 8, no. 5, pp. 606–612, 1999.
[22] A. Waqas, X. Qin, J. Xiong, H. Wang, and C. Zheng, "Optimization of process parameters to improve the effective area of deposition in GMAW-based additive manufacturing and its mechanical and microstructural analysis," *Metals*, vol. 9, no. 7, p. 775, 2019.
[23] S.-J. Lee, J.-S. Park, and Y.-K. Lee, "Effect of austenite grain size on the transformation kinetics of upper and lower bainite in a low-alloy steel," *Scripta Materialia*, vol. 59, no. 1, pp. 87–90, 2008.
[24] Z. J. Luo, J. C. Shen, H. Su, Y. H. Ding, C. F. Yang, and X. Zhu, "Effect of substructure on toughness of lath martensite/bainite mixed structure in low-carbon steels," *Journal of Iron and Steel Research*, vol. 17, no. 11, pp. 40–48, 2010.
[25] M. Fushimi, K. Keira, and H. Chikaraishi, "Nippon steel technic," *Forestry Report*, vol. 66, pp. 29–36, 1995.
[26] M. W. Tong, Z. X. Yuan, K. G. Zhang, and X. L. Rui, *Journal of Iron and Steel Research*, vol. 18, no. S1-2, pp. 903–907, 2011.
[27] E. J. Pavlina and C. J. Van Tyne, "Correlation of yield strength and tensile strength with hardness for steels," *Journal of Materials Engineering and Performance*, vol. 17, no. 6, pp. 888–893, 2008.
[28] B. Cui, Y. Peng, L. Zhao, M. D. Peng, T. B. An, and C. Y. Ma, "Effect of heat input on microstructure and toughness of coarse grained heat affected zone of Q890 steel," *ISIS Int*, vol. 56, no. 1, pp. 132–139, 2016.
[29] L. Sun, F. Jiang, R. Huang, D. Yuan, C. Guo, and J. Wang, "Anisotropic mechanical properties and deformation behavior of low-carbon high-strength steel component fabricated by wire and arc additive manufacturing," *Materials Science and Engineering A*, vol. 787, Article ID 139514, 2020.
[30] G. Mao, R. Cao, J. Yang et al., "Effect of nickel contents on the microstructure and mechanical properties for low-carbon bainitic weld metals," *Journal of Materials Engineering and Performance*, vol. 26, no. 5, pp. 2057–2071, 2017.